doi:10.14311/ppt.2025.3.176
Plasma Physics and Technology **12**(3):176–181, 2025

MAGNETOHYDRODYNAMIC MODELING OF DIRECT CURRENT ARC INTERRUPTION IN A LOW-VOLTAGE SWITCH

S. Kimpeler[a,*], F. Mingers[a], V. West[a], D. Fuhrmann[b], A. Tönnesmann[b], W. Leterme[a]

[a] *IAEW at RWTH Aachen University, 52062 Aachen, Germany*

[b] *Pierburg GmbH, 41460 Neuss, Germany*

[*] s.kimpeler@iaew.rwth-aachen.de

Abstract. This paper proposes a magnetohydrodynamic arc model for direct current arc interruption simulation in a low-voltage switch with a contact bridge design. Arc voltage and current for the interruption of an initial current and voltage in the 800 V and 800 A range are compared and differences discussed between the simulation and an experiment. The arc is successfully quenched in the simulation, but discrepancies between simulation and experiment may be attributable to erosion modeling.

Keywords: direct current arc, magnetohydrodynamic arc simulation, arc interruption, low-voltage switch, DC contactor.

1. Introduction

Higher battery voltages of up to 800 V are being used to enable increased power flows to achieve faster charging times of battery electric vehicles (BEVs) [1]. These increased voltages and power flows introduce new challenges for mechanical direct current (DC) switches, as they must oppose the battery voltage to extinguish the arc that is created when opening the current-carrying contacts during a switching operation. The switch has to drive and maintained the arc voltage above the battery voltage until the current reaches current zero. Therefore, in order to design efficient and reliable DC switches capable of handling the increased power flows and voltages, a fundamental understanding of DC arcs is essential [2].

Experimental measurements of relevant parameters on electric arcs are challenging due to arc core temperatures typically exceeding 10 000 K, high local pressure gradients and arc dynamics. Therefore, spatially and temporally resolved magnetohydrodynamic (MHD) arc models offer a promising addition to experimental investigations and may reduce time and expenses involved in the development of DC switches [3].

The design principle and functioning of a DC switch depends on the application and its requirements. Requirements include the voltage level, maximum rated interruptible current, number of switching cycles, low operating current losses, size and cost of the switch [4]. Traditional alternating current (AC) switch designs do not meet the requirements of BEVs, since suitable switches have to be compact in size and weight, allow a comparably high number of switching cycles, and have to be able to interrupt comparably high DC currents at a rated voltage of 800 V. Designs differing from typical AC designs are explored in order to meet these challenges, with one being the so-called contact bridge design (Figure 1) [5–7].

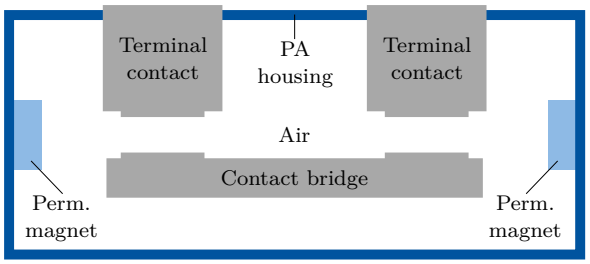

Figure 1. Schematic side view of a switch with a contact bridge design and its key components.

Due to the variety of switch designs and operating principles, MHD arc simulations must be parameterized and verified for each individual switch design. Previous works have focused on modeling switching arcs in AC switches for various switch designs and function principles [8–10]. The applicability of these existing parameterizations to a low-voltage switch with a contact bridge design is still unknown. The existing literature on contact bridge design models has focused on individual modeling aspects such as distribution of magnetic field [11], actuator design [12], and current zero crossing of an AC current [13], without consideration of arc interruption for DC current.

In this work, an MHD arc model for simulation of DC current interruption in a low-voltage switch with a contact bridge design is developed. The interruption performance of the simulation is evaluated for a typical operation profile and compared to an experimental result with possible explanations for deviations between experiment and simulation being discussed. We present the switch geometry and model setup in Chapter 2 and explain the method in Chapter 3. In Chapter 4, we present and discuss the results. Finally, we give a conclusion in Chapter 5.

2. Arc model

2.1. Geometry

The geometry consists of two terminal contacts, which are connected by a contact bridge (Figure 1). When opening the contacts, the contact bridge moves away from the terminal contacts igniting two arcs. Permanent magnets are located across the contact gap, thus creating a magnetic field. This magnetic field is orthogonal to the arcs and drives the arcs out of the contact gap. The arcing chamber is filled with air at atmospheric pressure and enclosed in a polyamide (PA) housing. The geometry is surrounded by an air box with the dimension 70 mm × 53 mm × 33 mm.

2.2. Governing equations

An MHD approach with the assumption of local thermodynamic equilibrium is used to model the thermal plasma with turbulence being accounted for by the realizable two-layer k-ϵ model. Therefore, the equation of mass is considered as follows:

$$\frac{\partial \rho}{\partial t} + \nabla \cdot (\rho \bar{\mathbf{v}}) = S_{\mathrm{m,PA}} \tag{1}$$

with ρ representing the gas density, $\bar{\mathbf{v}}$ the mean velocity and $S_{\mathrm{m,PA}}$ the polymer ablation mass source term. The momentum equations are represented by:

$$\frac{\partial (\rho \bar{\mathbf{v}})}{\partial t} + \nabla \cdot (\rho \bar{\mathbf{v}} \otimes \bar{\mathbf{v}}) = \nabla \cdot (\bar{p}_{\mathrm{mod}} \mathbf{I}) + \nabla \cdot \left(\bar{\mathbf{T}} + \bar{\mathbf{T}}_{\mathrm{RANS}}\right) + \mathbf{f}_{\mathrm{L}} \tag{2}$$

with the modified mean pressure $\bar{p}_{\mathrm{mod}} = \bar{p} + \frac{2}{3}\rho k$, where $\bar{p}$ is the mean pressure and k the turbulent kinetic energy. Furthermore, $\mathbf{I}$ is the identity tensor, $\bar{\mathbf{T}}$ the mean viscous stress tensor, $\bar{\mathbf{T}}_{\mathrm{RANS}}$ the stress tensor and $\mathbf{f}_{\mathrm{L}}$ the Lorentz force density. The energy equation is:

$$\nabla \cdot \left[\rho \bar{E} \bar{\mathbf{v}} + \bar{p}_{\mathrm{mod}} \bar{\mathbf{v}} - \left(\bar{\mathbf{T}} + \bar{\mathbf{T}}_{\mathrm{RANS}}\right) \bar{\mathbf{v}} + \bar{\mathbf{q}}\right] + \frac{\partial \rho \bar{E}}{\partial t} = S_{\mathrm{j}} + S_{\mathrm{e,PA}} - \nabla \cdot \mathbf{q}_{\mathrm{rad}} \tag{3}$$

with the mean total energy $\bar{E}$, the mean and radiative heat fluxes $\bar{\mathbf{q}}$ and $\mathbf{q}_{\mathrm{rad}}$ and the source terms for the Joule heating S_{j} and polymer ablation $S_{\mathrm{e,PA}}$. The transport equation for the kinetic energy is:

$$\frac{\partial (\rho k)}{\partial t} + \nabla \cdot (\rho k \bar{\mathbf{v}}) = \nabla \cdot \left[\left(\eta + \frac{\eta_{\mathrm{t}}}{\sigma_{\mathrm{k}}}\right) \nabla \cdot k\right] + P_{\mathrm{k}} - \rho (\varepsilon - \varepsilon_0) \tag{4}$$

with the dynamic and turbulent eddy viscosity η and η_{t}. Finally, the transport equation for the turbulent dissipation rate ε is:

$$\frac{\partial (\rho \varepsilon)}{\partial t} + \nabla \cdot (\rho \varepsilon \bar{\mathbf{v}}) = \nabla \cdot \left[\left(\eta + \frac{\eta_{\mathrm{t}}}{\sigma_{\varepsilon}}\right) \nabla \cdot \varepsilon\right] + \frac{1}{T_{\mathrm{e}}} C_{\mathrm{e1}} P_{\varepsilon} - C_{\mathrm{e2}} f_2 \rho \left(\frac{\varepsilon}{T_{\mathrm{e}}} - \frac{\varepsilon_0}{T_0}\right) \tag{5}$$

Band	λ_l (nm)	λ_u (nm)
1	33.3	85.3
2	85.3	91.2
3	91.2	102
4	102	160.5
5	160.5	194.5
6	194.5	324.8
7	324.8	10 000

Table 1. Band limits.

with the k-ϵ model turbulence value ε_0, coefficients σ_{ε}, σ_{k}, C_{e1}, and C_{e2}, production terms P_{ε}, and P_{k}, damping function f_2, specific and large-eddy time scale T_0 and T_{e}.

The equations are coupled with the equation for the electric scalar potential ϕ and the equations for the magnetic vector potential $\mathbf{A}$ via the temperature and pressure dependent electrical conductivity σ, Lorentz force $\mathbf{f}_{\mathrm{L}} = \mathbf{J} \times \mathbf{B}$ and Joule heating $S_{\mathrm{j}} = \mathbf{J} \cdot \mathbf{E}$ with $\mathbf{J} = -\sigma \nabla \phi$ being the electric current density, $\mathbf{E} = -\nabla \phi - \frac{\partial \mathbf{A}}{\partial t}$ the electric field, and $\mathbf{B} = \nabla \times \mathbf{A}$ the magnetic field. The electric potential equation is:

$$-\nabla \cdot (\sigma \nabla \phi) = \nabla (\sigma \frac{\partial \mathbf{A}}{\partial t}) + \nabla \cdot \mathbf{J}_{\mathrm{ex}} \tag{6}$$

with $\mathbf{J}_{\mathrm{ex}} = \mathbf{J}_{\mathrm{bc}} + \nabla \times \frac{1}{\mu} \mathbf{B}_{\mathrm{r}}$ accounting for external electric current density sources which are electric current densities defined as boundary condition $\mathbf{J}_{\mathrm{bc}}$ (see section 2.3) and from the permanent magnets with $\mathbf{B}_{\mathrm{r}}$ representing the permanent magnet remanent magnetic flux density and $\mu = \mu_{\mathrm{r}} \mu_0$ the magnetic permeability dependent on the vacuum magnetic permeability μ_0 and the relative magnetic permeability μ_{r}. The magnetic vector potential equation is as follows:

$$\nabla \times \frac{1}{\mu} \nabla \times \mathbf{A} + \sigma \frac{\partial \mathbf{A}}{\partial t} = -\sigma \nabla \phi + \mathbf{J}_{\mathrm{ex}}. \tag{7}$$

Radiation is modeled spatially and spectrally independent. The radiative heat flux is solved by the discrete ordinate method and the spectral part is simplified using mean absorption coefficients that are calculated for seven bands (see Table 1) using the Planck mean [14]. The band limits are derived using the method from [15].

Polymer ablation is modeled as in [9, 15]. The ablation mass source term is:

$$S_{\mathrm{m,PA}} = \frac{q_{\mathrm{w}} A_{\mathrm{w}}}{V_{\mathrm{c}} \Delta h_{\mathrm{eff,PA}}} \tag{8}$$

with q_{w} being the net radiative wall heat flux, A_{w} the face area of the cell, and V_{c} the volume of the cell where the source term is applied. The sum of the bonding energies of PA is used for estimating the effective ablation enthalpy $\Delta h_{\mathrm{eff,PA}} = 12.5\,\mathrm{MJ\,kg^{-1}}$ [15, 16]. The energy source term is calculated from the PA enthalpy difference of the solid and vaporized PA at

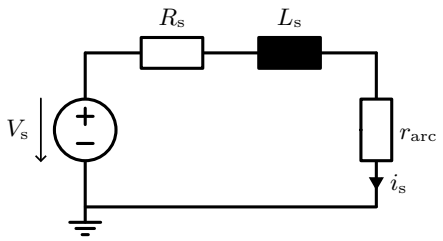

Figure 2. Equivalent electric circuit diagram.

the local pressure p and their respective temperatures $T_{\text{solid,PA}}$ and $T_{\text{vapor,PA}}$:

$$S_{\text{e,PA}} = S_{\text{m,PA}}(h_{\text{PA}}\,(p, T_{\text{vapor,PA}}) - h_{\text{PA}}\,(p, T_{\text{solid,PA}})) \quad (9)$$

The source terms are applied to the boundary layer in the air at the interface to the PA housing. The propagation of the PA vapor is modeled with the transport equation for the mass fraction ϕ_{PA}:

$$\frac{\partial}{\partial t}(\rho\phi_{\text{PA}}) + \nabla \cdot (\rho\phi_{\text{PA}}\bar{\mathbf{v}}) = \nabla \cdot \mathbf{j}_{\text{PA}} + S_{\text{m,PA}} \quad (10)$$

Contact erosion is neglected due to numerical stability reasons.

All equations are solved for finite volumes except the magnetic vector potential which is solved for finite elements. The electric current density and magnetic field are interpolated between the tetrahedral mesh for the finite elements and the polyhedral mesh for the finite volumes via the method of least squares.

2.3. Boundary and initial conditions

For the DC switch investigated in this paper, only the initial current and the system voltage are specified as boundary conditions, with the aim of investigating arc interruption behavior of the switch. To calculate the arc model input current corresponding to the model arc voltage at each time step, the arc model is coupled with an electric circuit model. The coupling is achieved by passing the arc voltage of the arc model v_{arc} as input parameter to the electric circuit model and the current of the system i_s in the electric circuit model as input parameter to the arc model. The current is set as external electric current density flux in the electric potential equation at one electrode in the arc model, while the other electrode serves as reference potential with the eletric potential being set to 0 V. Since the current-voltage-characteristic of a switching arc is essentially ohmic [17], the arc is represented by a resistor with the resistance $r_{\text{arc}} = \frac{v_{\text{arc}}}{i_s}$ in the electric circuit model. The circuit is completed by a voltage source representing the system voltage V_s, the electrical system inductance L_s and resistance R_s (Figure 2). After the initialization of the arc model, the arc voltage typically exhibits a steep voltage slope due to the numerical equations stabilizing. This is a consequence of the model's initialization process and does not reflect the behavior of physical arcs. Therefore, the MHD arc model and electric circuit model are only coupled once the model arc voltage has stabilized after a number of time steps.

The current density-dependent voltage characteristic from [8] is used for implementing the fall voltage:

$$V_{\text{fall}} = \frac{c_a J_A + c_b {J_A}^2}{c_c + {J_A}^2} \quad (11)$$

The characteristic curve depends on the electric current density J_A at the interface between electrode and plasma and the coefficients $c_a = 3\times10^8$, $c_c = 1.1\times10^{14}$ and c_b with $c_b = 5$ at the anode and $c_b = 10$ at the cathode [8]. The characteristic curve is implemented at the electrode-plasma interfaces.

Contact motion is implemented via morphing and remeshing. The mesh is morphed until either the cell volume or cell quality falls below a defined threshold which triggers a remeshing. Additionally, the mesh is remeshed at least every 300 time steps to ensure a generally high mesh quality. Contact bridge opening velocity is $1\,\text{m}\,\text{s}^{-1}$, based on the experimental measurements.

The arc formation with its transition from molten metal bridge to metal vapor arc is out of scope for this paper. However, the transition from a metal vapor arc to a gas arc occurs at around 0.01 mm to 1 mm contact distance depending on the contact material and ionization energy of the gas atoms [18]. Therefore, the initial contact gap distance is set to 0.1 mm with the initial contact gap being filled with copper vapor to represent the metal vapor arc. The transport equation for the copper vapor propagation is analogue to the PA vapor propagation (see (10)).

The thermodynamic and transport properties of air-PA-copper mixture are modeled dependent on temperature, pressure, copper mass fraction, and PA mass fraction with the data from [19].

The arc is initialized with a temperature profile [20] that is applied to a channel between the electrodes. The temperature profile has a core temperature of 15 000 K, with the temperature decreasing to 300 K ambient temperature in radial direction. The time step size is 1 µs.

The model is setup in the software framework Simcenter STAR-CCM+.

3. Method

The simulated arc behavior is investigated using a typical operation profile for a BEV with a source voltage in the range of 800 V and an initial current in the range of 800 A. Arc voltage v_{arc} and current i_{arc} of the simulation are compared to those of an exemplary experiment using the same operation profile. To evaluate and discuss the arc behavior in the simulation, the mean pressure in the arc chamber p_{acm} is visualized alongside the arc core location in the contact gap. Mean pressure and arc core location are not determined in the experiment.

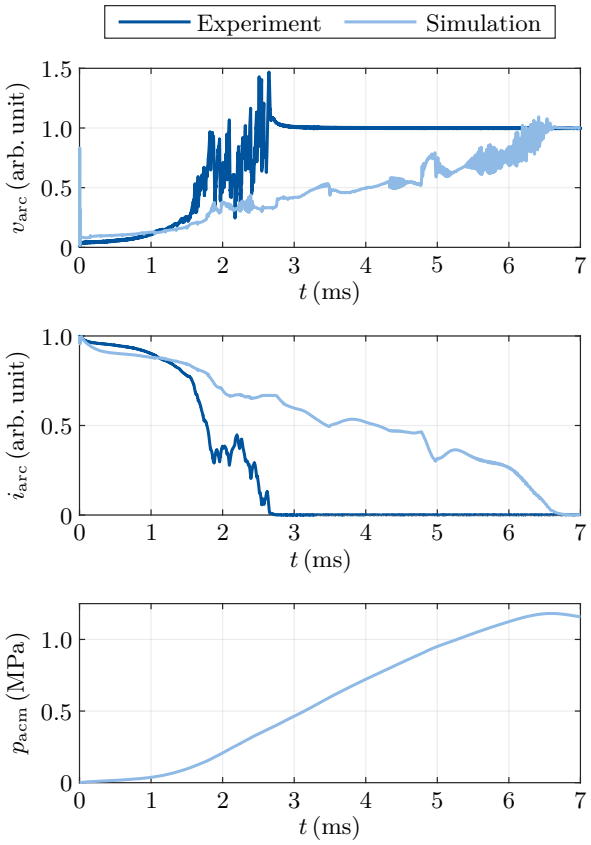

Figure 3. Experimental and simulation arc voltage v_{arc} (top) and current i_{arc} (center) over time normalized for the source voltage and inital current of the operation profile. Simulation mean pressure in arc chamber p_{acm} over time (bottom).

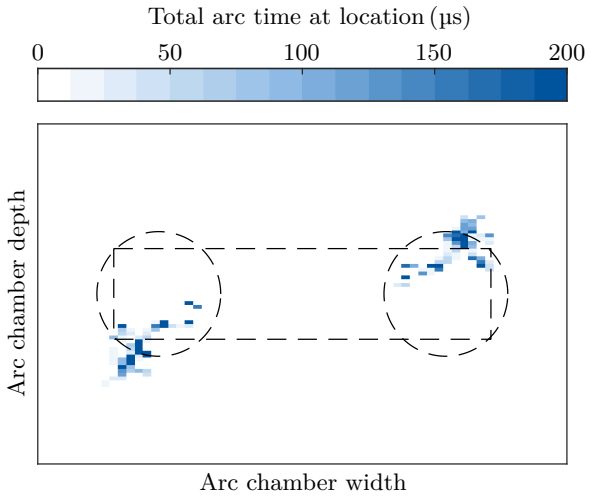

Figure 4. Top view of arc chamber with the total arc core time at location in the center plane of the contact gap. The terminal contacts above the center plane are indicated by the black dash circles and the contact bridge below the center plane is indicated by the black dash rectangle.

To determine the arc core location in the center plane of the contact gap, the point of maximum current density is used. For visualization purposes, the plane is divided into 50 equally sized regions in each dimension, and the number of maximum current density points in each region is counted for each arc, respectively. Since each point counted corresponds to one time step, this also visualizes the cumulated total arc time at each location.

4. Results and discussion

The arc ignition in simulation and experiment occurs at 0 ms. The initial arc voltage in the simulation is twice as much as the arc voltage of the experiment (Figure 3). The difference can be attributed to the initial contact gap and the constant bridge opening velocity in the simulation, as opposed to the experiment where contacts start closed and the bridge must first accelerate. This results in a larger contact gap in the simulation compared to the experiment until approximately 1 ms, leading to a higher arc voltage.

At approximately 1.5 ms, the experimental arc voltage increases rapidly. At this point in time the arcs are moved out of the contact gap, elongating and thus increasing the arc voltage. However, once the arc voltage is higher than the breakdown voltage of the contact gap, the arcs reignites in the contact gap as indicated by a steep decrease in experimental arc voltage sometimes by as much as 50 % e.g. at approximately 1.9 ms. From this arc voltage decrease in the experiment, we can approximate that the arcs elongate at least twice the length of the contact distance as can be seen in arc recordings in similar geometries [11, 21, 22]. This arc behavior is not observed in the arc simulation. When the arcs are moved out of the contact gap in the simulation at approximately 1.5 ms, no significant increase in arc voltage is discernible. This is possibly due to a—compared to the experiment—shorter elongation of the arcs. This is illustrated by the heat map of the arc locations in the center plane of the contact gap (Figure 4). While the arcs move to the edge of the contacts, as is expected due to the Lorentz forces of the permanent magnets and the magnetic field of the other respective arc, the distance of the arc cores to the contacts is small compared to the overall distance to the housings wall.

The arc elongation increases the overall mean arc voltage. Hence, the experimental arc current is decreased to 40 % of the initial current by 2 ms, whereas the simulated arc current is only decreased to 70 % by that time. A possible explanation for the insufficient elongation of the arcs in the simulation is the absence of contact erosion in the simulation. Contact vapor strongly increases emission from the arc core [23], thus arc movement might be increased. Furthermore, the velocity of the contact vapor due to erosion processes [24] might also further increase arc movement and thus arc elongation.

During the arcing time, the arc influence leads to polymer ablation from the housing walls and contact erosion. This conversion of solid to gaseous material leads to a continues pressure rise in the arc cham-

ber, thus decreasing electrical conductivity and subsequently an increase in arc voltage. Furthermore, the PA and contact vapor alter the plasma composition. PA contains hydrogen that is released during the ablation process. Hydrogen, having a comparatively high thermal conductivity, facilitates faster heat distribution in the arc chamber and extracts energy from the arc core, aiding in arc quenching [25, 26]. This effect is enhanced by the contact metal vapor increasing radiation emission from the arc core, thus further extracting energy from the arc core [23]. The cumulative effect of these processes can be observed in the increasing mean arc voltage over time in the experiment. The simulation arc voltage also exhibits this effect, albeit at a slower rate. Again, the explanation of this discrepancy may lie in the absence of erosion and its influences in the arc model. Another contributing factor might be the lower elongation of the simulation arcs and thus greater distance to the polymer housing walls compared to the experimental arcs, which might lead to lower ablation rates in the simulation compared to the experiment. However, an overall increase in pressure can be observed (Figure 3).

In the experiment, the processes described lead to a decreasing current with current zero being reached at approximately 2.75 ms. Due to the overall slower increase in simulation arc voltage, the time to reach current zero in the simulation is with approximately 6.8 ms higher compared to the experiment.

5. Conclusion

The proposed MHD arc model for a low-voltage switch with contact bridge design is able to successfully quench a DC fault current of a typical operational profile in the 800 V and 800 A range. However, the current interruption time is higher by a factor of 2.5 compared to the experiment. Overall, the simulation shows promising results. However, further insights are needed regarding the insufficient arc elongation of the simulation. Future development of the model aims to include contact erosion, which is currently considered the most influential phenomenon that explains the discrepancy between simulation and experiment.

Acknowledgements

Simulations were performed with computing resources granted by RWTH Aachen University under project rwth1424.

References

[1] C. Jung. Power up with 800-V systems: The benefits of upgrading voltage power for battery-electric passenger vehicles. *IEEE Electrification Magazine*, 5:53–58, 2017. doi:10.1109/MELE.2016.2644560.

[2] M. Lindmayer, editor. *Schaltgeräte: Grundlagen, Aufbau, Wirkungsweise*. Springer Berlin Heidelberg, 1987.

[3] A. Gleizes, J. J. Gonzalez, and P. Freton. Thermal plasma modelling. *Journal of Physics D: Applied Physics*, 38:R153–R183, 2005. doi:10.1088/0022-3727/38/9/R01.

[4] K. Niayesh and M. Runde. *Power Switching Components*. Springer International Publishing, 2017.

[5] T. Schrank, E.-D. Wilkening, M. Kurrat, et al. Breaking performance of a circuit breaker influenced by a permanent magnetic field at dc voltages up to 450 V. In *26th International Conference on Electrical Contacts (ICEC 2012)*, pages 35–40, 2012. doi:10.1049/cp.2012.0618.

[6] H. Köpf. *Schalten von Gleichströmen in automobilen HV-Bordnetzen bis 500 V, unter Berücksichtigung der Lichtbogenwanderung im Doppelkontaktsystem*. PhD thesis, Technische Universität Braunschweig, 2018.

[7] X. Liu, X. Huang, and Q. Cao. Simulation and experimental analysis of dc arc characteristics in different gas conditions. *IEEE Transactions on Plasma Science*, 49:1062–1071, 2021. doi:10.1109/TPS.2021.3054657.

[8] C. Rümpler. *Lichtbogensimulation für Niederspannungsschaltgeräte*. PhD thesis, Technische Universität Ilmenau, 2009.

[9] F. Reichert. *Numerische Simulation strömungsmechanischer Vorgänge in SF6-Hochspannungsleistungsschaltern*. habilitation, Technische Universität Ilmenau, 2015.

[10] R. Fuchs. *Numerical Modeling and Simulation of Electric Arcs*. PhD thesis, ETH Zürich, 2021. doi:10.3929/ethz-b-000489867.

[11] S. Gortschakow, D. Gonzalez, S. Yu, and F. Werner. 3d analysis of low-voltage gas-filled dc switch using simplified arc model. *Plasma Physics and Technology*, pages 65–68, 2019. doi:10.14311/ppt.2019.1.65.

[12] R. Fuchs and P. Kloc. Numerical simulation of dc-contactor in hydrogen-nitrogen gas capsule. In *23rd International Conference on Gas Discharges and their Applications*, pages 112–115, 2023.

[13] R. Chechare, C. Rümpler, A. Mujawar, and K. Bednarski. Model-based optimization of the switching performance of a switch disconnector. *Plasma Physics and Technology*, 10:40–46, 2023. doi:10.14311/ppt.2023.1.40.

[14] P. Kloc, V. Aubrecht, M. Bartlova, and R. Fuchs. Comparison of mean absorption methods for radiation transfer models in air plasma at various pressures. *Plasma Chemistry and Plasma Processing*, 43:429–447, 2023. doi:10.1007/s11090-022-10304-9.

[15] S. Kimpeler, F. Mingers, V. West, et al. Influence of polyamide 6.6 ablation on direct current arcs – experiment and simulation: Unpublished journal article, 2025.

[16] C. Rümpler, H. Stammberger, and A. Zacharias. Low-voltage arc simulation with out-gassing polymers. In *2011 IEEE 57th Holm Conference on Electrical Contacts (Holm)*, pages 1–8, 2011. doi:10.1109/HOLM.2011.6034770.

[17] M. I. Boulos, P. L. Fauchais, and E. Pfender, editors. Springer International Publishing and Imprint Springer, 1st ed. 2023 edition edition, 2023. doi:10.1007/978-3-030-84936-8.

[18] E. Vinaricky, K.-H. Schröder, and J. Weiser, editors. *Elektrische Kontakte, Werkstoffe und Anwendungen*. Springer Berlin Heidelberg, Berlin, Heidelberg, 2016. doi:10.1007/978-3-642-45427-1.

[19] Y. Cressault, S. Kimpeler, A. Moser, and P. Teulet. Thermophysical properties of air-pa66-copper plasmas for low-voltage direct current switches. *Plasma Physics and Technology*, 10:52–55, 2023. doi:10.14311/ppt.2023.1.52.

[20] P. Kloc, V. Aubrecht, and M. Bartlova. Numerically optimized band boundaries of planck mean absorption coefficients in air plasma. *Journal of Physics D: Applied Physics*, 50:305201, 2017. doi:10.1088/1361-6463/aa7627.

[21] D. Gonzalez, S. Gortschakow, S. Yu, and F. Werner. Investigation of the arc characteristics of switching dc arcs on hydrogen containing gas mixtures. *Plasma Physics and Technology*, 6:69–72, 2019. doi:10.14311/ppt.2019.1.69.

[22] D. Gonzalez, S. Gortschakow, R. Methling, et al. Switching behavior of a gas-filled model dc-contactor under different conditions. *IEEE Transactions on Plasma Science*, 48:2515–2522, 2020. doi:10.1109/TPS.2020.3003525.

[23] C. B. Ruchti and L. Niemeyer. Ablation controlled arcs. *IEEE Transactions on Plasma Science*, 14:423–434, 1986. doi:10.1109/TPS.1986.4316570.

[24] P. G. Slade, editor. CRC Press Taylor & Francis Group, Boca Raton and London and New York, second edition, first issued in paperback edition edition, 2017.

[25] E. Jonsson, M. Runde, G. Dominguez, et al. Comparative study of arc-quenching capabilities of different ablation materials. *IEEE Transactions on Power Delivery*, 28:2065–2070, 2013. doi:10.1109/TPWRD.2012.2227834.

[26] H. Taxt, K. Niayesh, and M. Runde. Medium-voltage load current interruption in the presence of ablating polymer material. *IEEE Transactions on Power Delivery*, 33:2535–2540, 2018. doi:10.1109/TPWRD.2018.2803165.